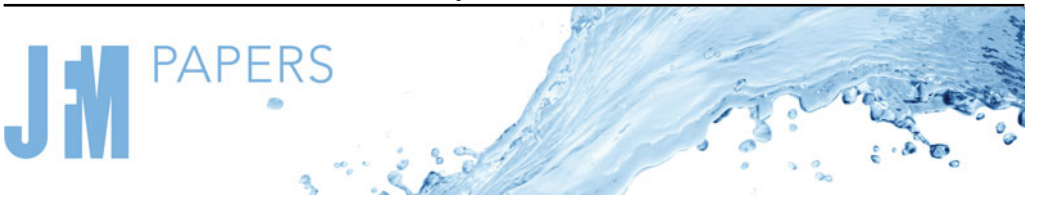
J. Fluid Mech. (2026), *vol.* 1042, A9, doi:10.1017/jfm.2026.11965



Hydrodynamic interactions characterise active rheology of soft microswimmer suspensions

Kiyoto Kubo[1], **Toshihiro Omori**[1] **and Takuji Ishikawa**[1,2]

[1]Department of Finemechanics, Tohoku University, Sendai 980-8579, Japan

[2]Department of Biomedical Engineering, Tohoku University, Sendai 980-8579, Japan

Corresponding authors: Kiyoto Kubo, kiyoto.kubo.q5@dc.tohoku.ac.jp; Toshihiro Omori omori@tohoku.ac.jp

(Received 19 November 2025 UTC; revised 3 June 2026 UTC; accepted 20 July 2026 UTC)

Swimming microorganisms dynamically respond to their external environment, resulting in self-organised collective behaviour. To accurately predict the flow field at the continuum scale, it is essential to understand the rheological properties of active suspensions. Microorganisms in nature exhibit a wide range of deformabilities, and former studies have reported that they play an important role in hydrodynamic interactions. However, the effect of cell deformability on suspension rheology has not yet been clarified. In this study, we developed a soft microswimmer model to represent general swimming microorganisms to investigate rheological properties such as apparent viscosity and normal stress differences of their suspensions. The model consisted of a capsule with a hyperelastic membrane and propelled itself by a torque distribution modelling the ciliary activity of a ciliate. Our results demonstrated that interparticle hydrodynamic interaction is a critical factor inducing symmetry breaking in the time-averaged orientational distribution in the low shear flow. For the ellipsoidal swimmers, these interactions promote orientational distribution biased towards the elongational direction, resulting in inherent viscosity variation in microbial suspensions. In addition, this orientational distribution is distinctly different from that observed in solitary swimmers, causing the significant reduction (increase) in the apparent viscosity for the pusher (puller). Analysis varying membrane deformability showed that the softer membrane is less likely to exhibit the effects of the active stress on specific viscosity. These findings demonstrate the important role of elastohydrodynamic interactions between swimmers in suspension rheology and support the development of continuum models for complex microbial systems.

Key words: micro-organism dynamics, swimming/flying, capsule/cell dynamics

© The Author(s), 2026. Published by Cambridge University Press. This is an Open Access article, distributed under the terms of the Creative Commons Attribution-NonCommercial-ShareAlike licence (https://creativecommons.org/licenses/by-nc-sa/4.0/), which permits non-commercial re-use, distribution, and reproduction in any medium, provided the same Creative Commons licence is used to distribute the re-used or adapted article and the original article is properly cited. The written permission of Cambridge University Press or the rights holder(s) must be obtained prior to any commercial use.

https://doi.org/10.1017/jfm.2026.11965 Published online by Cambridge University Press

1. Introduction

Macroscopic rheological properties induced by the presence of internal particles are important for understanding and predicting the complex flow of suspensions. The earliest theoretical framework that connects microscopic particles and macroscopic rheological characteristics was established by Einstein (1906). He analysed the hydrodynamic effect of a rigid sphere in a simple shear flow and formulated the apparent viscosity μ_a as a linear function of the particle volume fraction c: $\mu_a = \mu(1 + 5c/2)$. By the 1970s, Batchelor (1970) had systematised the relationship between microscopic particle motions and macroscopic rheology as a systematic stress system. When force-free particles are suspended in a fluid, the bulk stress can be described by adding the particle stress, $\boldsymbol{\Sigma}^{(p)}$, to the constitutive law of the fluid as a linear sum. Under force-free conditions, $\boldsymbol{\Sigma}^{(p)}$ is typically evaluated by the stresslet $\boldsymbol{S}$ generated by suspended particles (see (2.23)). It was shown that the bulk apparent viscosity in the dilute regime derived from the stresslet of particles under shear flow agrees with Einstein's viscosity law. Batchelor & Green (1972) extended this formulation by incorporating the second-order term $O(c^2)$ which arises from two-body hydrodynamic interactions between particles. Bossis & Brady (1984) developed a general method for numerically simulating the dynamics of many interacting particles, known as the Stokesian dynamics, which is capable of simulating more concentrated regimes by accounting for both short-range lubrication forces and long-range hydrodynamic interactions. This approach was comprehensively summarised in the review article by Brady & Bossis (1988), and has been widely used to investigate the effects of microstructure and interparticle forces on the rheological properties of suspensions. According to Bossis, Brady and their colleagues' work, the balance between hydrodynamic and interparticle forces determines the anisotropy of the microstructure, which profoundly impacts the emergence of non-zero normal stress differences (Brady & Bossis 1985; Brady & Morris 1997; Sierou & Brady 2002). Additionally, the effects of colloidal forces, particle shapes and Brownian motions on particle stress have been intensively investigated and summarised in a number of review papers (Brenner 1974; Jeffrey & Acrivos 1976; Russel 1980; Guazzelli & Pouliquen 2018; Ness *et al.* 2022).

The rheology of suspensions is also of interest in active suspensions, with numerous analytical studies having been reported (Marchetti *et al.* 2013). In active suspensions, particles interact hydrodynamically with each other through the flow field generated by their self-propulsion. Ishikawa *et al.* (2006) carried out an analysis of the two-body interference problem by using a squirmer model, which is capable of representing a variety of flow fields caused by swimming microorganisms. It was reported that the hydrodynamic interactions between two squirmers lead them to approach each other and scatter their swimming directions after the collision. This hydrodynamic interaction plays a significant role in the microstructure formation in semi-dilute and dense suspensions, affecting the rheological changes. Ishikawa *et al.* (2008) successfully extended the squirmer into the Stokesian dynamics framework for concentrated suspensions and investigated their collective motions without any imposed flow. The squirmers demonstrate a weak aggregation and a global coherent polar order was observed for the weak puller and weak pusher types in the squirmer. In the shear flow, hydrodynamic interactions give rise to heterogeneous spatial distributions, both in the bulk suspension (Ishikawa & Pedley 2007; Guzmán & Soto 2019) and near boundary walls (Pagonabarraga & Llopis 2013). Recently, Ishikawa *et al.* (2025) have analysed the rheology of squirmer suspensions in Poiseuille flow, and found that the effective viscosity of bottom-heavy puller suspensions can be negative in the case of Poiseuille upflow.

https://doi.org/10.1017/jfm.2026.11965 Published online by Cambridge University Press

The rheology of active suspensions has also been the focus of experimental studies. In the 2010s, the experimental study conducted by López *et al.* (2015) measured the apparent viscosity of an *Escherichia coli* suspension by using a Couette rheometer and reported viscosity reduction. As a striking feature of this work, it was implied that the emergence of zero apparent viscosity (i.e. superfluid behaviour) occurs when the bacterial activity is sufficiently high. On the other hand, the viscosity measurement of *Chlamydomonas reinhardtii* suspension reported by Rafaï *et al.* (2010) exhibited greater viscosity than that of suspensions containing dead cells. These fascinating rheological features in the active systems are relevant to the active stress generated by the swimming activity of the particles. This active stress is strongly correlated with the orientation of the active particle (Hatwalne *et al.* 2004). Saintillan (2010) developed a model of active rod-like particles and elucidated the mechanism of rheological changes induced by the active stress. In simple shear flow, an active non-Brownian particle follows a motion similar to Jeffery orbits (Jeffery 1922), which means that the particle spends equal time oriented in the extensional and compressional quadrants of the shear flow. In this symmetrical circumstance, the active stress generated in each quadrant cancels out each other: there is no net contribution to apparent viscosity. Therefore, orientational symmetry breaking is essential for the emergence of inherent rheological behaviours in active suspensions. Saintillan (2010) pointed out that orientational fluctuations due to Brownian motion and run-and-tumbling motion in dilute suspensions are among the key factors that can break this symmetry. In addition to these orientation-related mechanisms, Ishikawa *et al.* (2021) discussed the influence of orientational anisotropy induced by the bottom-heavy cells on the bulk rheological properties. Recently, several experimental studies have suggested that the emergence of the negative viscosity increment in bacterial suspensions during rheometer measurements is correlated with the onset of collective swarming motions and resulting flows (Guo *et al.* 2018; Martinez *et al.* 2020). Details of the rheology of active suspensions are described in the review papers by Saintillan (2018) and Ishikawa (2025).

In nature, some microorganisms exhibit deformabilities which play important roles for cell–cell interactions (Matsui *et al.* 2020*a*) and collective motions (Menzel & Ohta 2012; Kubo *et al.* 2025), so the dynamics induced by the deformation of microorganisms has recently attracted considerable attention in the field of soft active matter physics. Ishikawa *et al.* (2016) developed a capsule-type microswimmer model based on the boundary-element–finite-element coupling method and Matsui *et al.* (2020*a*) conducted the two-body interference problem between these models to investigate deformation effects. In this model, a propulsive torque is employed to represent the active flow induced by the ciliary motion of swimming microorganisms. Although the soft swimmer follows almost the same trajectory as the rigid squirmer model before a face-to-face collision, the scattering angles after the collision become smaller due to deformation. In the analysis of the microstructures without any imposed flow performed by Kubo *et al.* (2025), the swimmer's deformation enables swimmers to more easily slip through each other, weakening the formation of orientational order through short-range hydrodynamic interactions. As a result, the polar order observed in rigid squirmer suspensions is less likely to form, particularly in suspensions of softer swimmers. Thus, there is the distinct difference between the dynamics of rigid and deformable swimmers.

In terms of the rheology, deformability has been reported to induce a shear-thinning effect on the viscosity of a passive capsule suspension, arising from a complex rotational dynamics such as alignment towards the vorticity axis and tank-treading motions in shear flows (Omori *et al.* 2012; Dupont *et al.* 2013; Zhang & Graham 2020). However, the effects of deformation on the rheology in active systems are seldom explored. Among them, the previous study conducted by Matsui *et al.* (2020*b*) investigated the rotational motion of the

https://doi.org/10.1017/jfm.2026.11965 Published online by Cambridge University Press

capsule-type swimmer in simple shear flow and a suspension rheology in the dilute limit. It was reported that the strong pusher (puller) swimmer finally aligns into the vorticity axis (shear plane) regardless of shear rates, whereas the weak swimmer, near the neutral type, switches this alignment direction depending on the balance between deformability and the shear rate. This difference in the alignment direction leads to a sign change in the second normal stress difference. On the other hand, apparent viscosity shows a shear-thinning property and the first normal stress difference becomes of positive sign, which are similar trends to those of passive capsule suspensions. However, these findings were obtained under the dilute limit (i.e. no cell–cell interactions). Although previous studies have demonstrated that deformability induces distinct changes in swimmer microstructures, a comprehensive understanding of the synergistic effects between deformation-induced reorientation and active stress in denser suspensions remains unclear.

Therefore, the objective of this study was to investigate the suspension rheology of soft microswimmers taking into account the elastohydrodynamic interactions between the swimmers. In this paper, a hyperelastic capsule with a thrust torque (Ishikawa *et al.* 2016; Matsui *et al.* 2020*b*) was employed as a soft swimmer. The basic equations and numerical method are presented in § 2. Rotational dynamics, shear viscosity and normal stress differences in the ideal dilute regime, as predicted by the solitary swimmer, are reported in § 3 and the Supplemental Material is available at https://doi.org/10.1017/jfm.2026.11965. In § 4, the suspension rheology in semi-dilute regimes including the influences of the cell–cell interaction is discussed. Furthermore, the effects of variations in swimmer shape and membrane deformability are examined. The summary of our findings and concluding remarks are presented in § 5.

2. Basic equations and numerical methods

This study used a similar framework to our previous studies (Ishikawa *et al.* 2016; Matsui *et al.* 2020*a*,*b*; Kubo *et al.* 2025). Thus, this paper only provides a brief overview of the numerical model and methodology here. For further details, please refer to our former papers.

2.1. *Soft microswimmer*

In this study, swimming microorganisms such as ciliates are modelled as soft microswimmers driven by propulsive torques. The original model was developed by Ishikawa *et al.* (2016) and expanded to two-body interactions by Matsui *et al.* (2020*b*). The model consists of a capsule with a two-dimensional hyperelastic thin membrane encasing an incompressible Newtonian fluid with the same viscosity μ and density ρ as the ambient fluid (cf. figure 1*a*). The reference shape of this model is a prolate with aspect ratio AR, varied from a sphere of radius a under constant volume (i.e. $4\pi a^3/3$). The thrust force at the cilium tip and the reaction force at the cilium root during the ciliary beating are modelled as the propulsive torque. Based on the assumption that the microbial ciliary beat occurs along the meridional direction, the propulsive torque is distributed as a vector oriented in the azimuthal direction over the torque surface A_t offset by a distance of ε from the membrane surface A. The propulsive torque per unit area in the reference state $\boldsymbol{L}_r$ is given by

$$\boldsymbol{L}_r = \left[L_0 + \kappa\left(\theta - \frac{\pi}{2}\right)\right]\boldsymbol{n} \times \boldsymbol{t}, \tag{2.1}$$

where κ determines the torque strength of the asymmetry, θ is the polar angle with respect to the orientation vector $\boldsymbol{e}$ defined by the posterior and anterior material points, $\boldsymbol{n}$ is the unit outward normal vector and $\boldsymbol{t}$ is the unit tangential vector in the θ direction. In our

https://doi.org/10.1017/jfm.2026.11965 Published online by Cambridge University Press

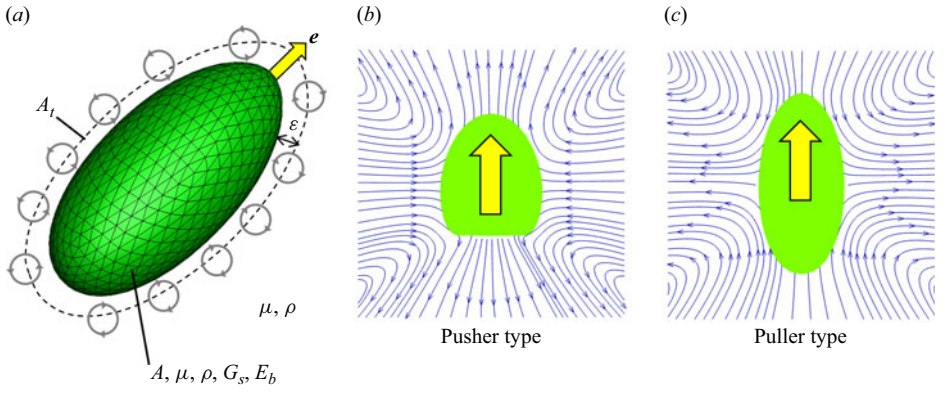


Figure 1. The ellipsoidal soft microswimmer model. (*a*) The soft swimmer is modelled by a capsule body composed of a hyperelastic thin membrane enclosing a Newtonian fluid with density ρ and viscosity μ. The surrounding fluid has the same ρ and μ. The mechanical properties of the membrane are represented by a shear elastic modulus G_s and bending modulus E_b. The propulsion torque expressing ciliary beating is set at the torque surface A_t defined as the surface slightly above the cell membrane A. The swimmer is discretised by 1280 triangular elements with 642 node points. (*b*,*c*) Flow fields created by the soft swimmer in the steady state. The swimmer deforms steady shape from an ellipsoidal shape with aspect ratio of 2 ($AR = 2$) due to propulsion torques. In this study, β is set to -1 for pusher swimmers and 1 for puller swimmers. Yellow arrows indicate swimming directions $\boldsymbol{e}$ and blue arrows are streamlines created by the swimmer.

model, $|\boldsymbol{L}_r|$ is assumed to be time invariant and is determined by adjusting the value of L_0 so that the swimmer in a steady state has a swimming speed U_0 under the free swimming condition. The swimmer in the reference state satisfies the torque-free condition on the overall torque surface due to the axisymmetric torque distribution. In contrast, in the deformed and steady states, this torque-free condition can be approximately maintained by locally adjusting the torque strength in response to the deformation, as follows:

$$\boldsymbol{L} = \frac{\mathrm{d}A_{t,r}}{\mathrm{d}A_t}\boldsymbol{L}_r, \tag{2.2}$$

where $\mathrm{d}A_{t,r}$ and $\mathrm{d}A_t$ are the local torque surface area in the reference and deformed states, respectively. This correction means that the number of cilia does not change with deformation.

The stresslet due to the presence of the capsule swimmer can be expressed by applying the reciprocal theorem proposed by Pozrikidis (1992) to the membrane interface

$$\boldsymbol{S} = \int \left[\frac{1}{2}(\boldsymbol{q}\boldsymbol{x} + \boldsymbol{x}\boldsymbol{q}) - \frac{1}{3}\boldsymbol{q}\cdot\boldsymbol{x}\boldsymbol{I}\right]\mathrm{d}A, \tag{2.3}$$

where $\boldsymbol{q}$ is a stress jump in the interfacial membrane with $\boldsymbol{n}$ at position $\boldsymbol{x}$, given by using viscous stress $\boldsymbol{\sigma}$ as

$$\boldsymbol{q}(\boldsymbol{x}) = [\boldsymbol{\sigma}_{out}(\boldsymbol{x}) - \boldsymbol{\sigma}_{in}(\boldsymbol{x})]\cdot\boldsymbol{n}(\boldsymbol{x}). \tag{2.4}$$

Our model employs the swimming mode β of the classical squirmer model (Blake 1971), such as pusher ($\beta < 0$) and puller ($\beta > 0$) types, to represent the differences in fluid motion of various swimming microorganisms. Here, β is calculated from the stresslet component in the swimming direction S_{ee} (Matsui *et al.* 2020*b*; Kubo *et al.* 2025)

$$\beta = \frac{S_{ee}}{4\pi\mu U_0 a^2}. \tag{2.5}$$

https://doi.org/10.1017/jfm.2026.11965 Published online by Cambridge University Press

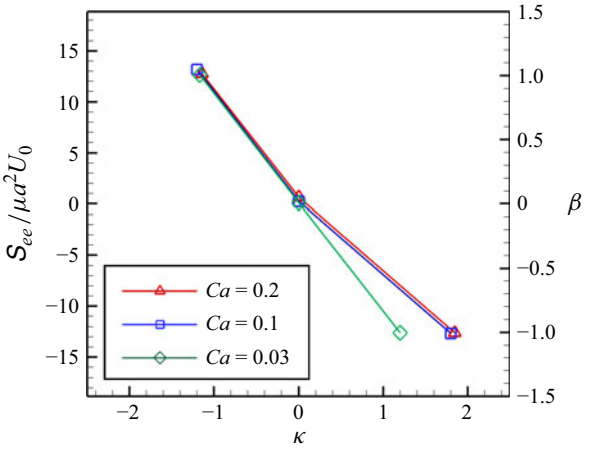


Figure 2. The relation between the asymmetry of torque strength κ, the stresslet component in the swimming direction S_{ee} and β of the soft swimmer with $AR = 2$ and each Ca. Here, Ca is the ratio between the viscous force due to swimming and the elastic force of the membrane defined by (2.22).

The value of β in our model is indirectly determined by adjusting κ, which creates the swimmer's anterior–posterior asymmetry. The correspondences between κ, β and S_{ee} for the ellipsoidal swimmers with $AR = 2$ are shown in figure 2. In this study, β was set to -1 for pushers and 1 for pullers.

2.2. *Membrane mechanics*

In order to describe local deformation on the membrane, our model employs thin-shell theory of capsules developed by Barthès-Biesel, Pozrikidis, and their co-workers, based on continuum mechanics. Here, we briefly explain the outline of thin-shell theory. For further details, please refer to Barthès-Biesel *et al.* (2002), Lac *et al.* (2004), Walter *et al.* (2010), Pozrikidis (2010).

To compute membrane tension, we first define the local curvilinear coordinate (ξ^1, ξ^2) on the two-dimensional membrane. The covariant basis vectors $\boldsymbol{A}_\alpha$ $(\alpha = 1, 2)$ in the reference state are defined as

$$\boldsymbol{A}_1 = \frac{\partial \boldsymbol{X}}{\partial \xi^1}, \qquad \boldsymbol{A}_2 = \frac{\partial \boldsymbol{X}}{\partial \xi^2}, \tag{2.6}$$

where $\boldsymbol{X}$ is the material position vector in the reference state. Similarly, the covariant basis vectors $\boldsymbol{a}_\alpha$ in the deformed state are given by

$$\boldsymbol{a}_1 = \frac{\partial \boldsymbol{x}}{\partial \xi^1}, \qquad \boldsymbol{a}_2 = \frac{\partial \boldsymbol{x}}{\partial \xi^2}. \tag{2.7}$$

The associated contravariant base vectors $\boldsymbol{A}^\alpha$ are defined by $\boldsymbol{A}^\alpha \cdot \boldsymbol{A}_\beta = \boldsymbol{\delta}^\alpha_\beta$ (likewise for $\boldsymbol{a}^\alpha$). Here, $\boldsymbol{\delta}^\alpha_\beta$ is the Kronecker tensor. The covariant and contravariant metric tensors are then defined as

$$A_{\alpha\beta} = \boldsymbol{A}_\alpha \cdot \boldsymbol{A}_\beta, \qquad A^{\alpha\beta} = \boldsymbol{A}^\alpha \cdot \boldsymbol{A}^\beta. \tag{2.8}$$

Applying the same rule to the deformed state, the covariant and contravariant metric tensors $a_{\alpha\beta}$ and $a^{\alpha\beta}$ in the deformed state are defined. The relation between the membrane material points in the reference and deformed states is described as follows:

$$\mathrm{d}\boldsymbol{x} = \boldsymbol{F}_s \cdot \mathrm{d}\boldsymbol{X}, \tag{2.9}$$

https://doi.org/10.1017/jfm.2026.11965 Published online by Cambridge University Press

where $\boldsymbol{F}_s$ is the surface deformation gradient tensor: $\boldsymbol{F}_s = \partial \boldsymbol{x}/\partial \boldsymbol{X} = \boldsymbol{a}_\alpha \otimes \boldsymbol{A}^\alpha$. Local deformation of the membrane can be described by the Green–Lagrange strain tensor as

$$\boldsymbol{E}_s = \frac{1}{2}\left[\boldsymbol{F}_s^T \boldsymbol{F}_s - (\boldsymbol{I} - \boldsymbol{N}\boldsymbol{N})\right], \tag{2.10}$$

and covariant form as

$$E_{s,\alpha\beta} = \frac{1}{2}\left(a_{\alpha\beta} - A_{\alpha\beta}\right)\boldsymbol{A}^\alpha \otimes \boldsymbol{A}^\beta. \tag{2.11}$$

The strain invariants are given by the principal extension ratios λ_1 and λ_2 as

$$\begin{aligned} I_1 &= 2tr\,\boldsymbol{E}_s \\ &= a_{\alpha\beta}A^{\alpha\beta} - 2 \\ &= \lambda_1^2 + \lambda_2^2 - 2, \end{aligned} \tag{2.12}$$

and

$$\begin{aligned} I_2 &= det\boldsymbol{C} - 1 \\ &= |a_{\alpha\beta}|\left|A^{\alpha\beta}\right| - 1 \\ &= \lambda_1^2\lambda_2^2 - 1 \\ &= J_s^2 - 1, \end{aligned} \tag{2.13}$$

where $\boldsymbol{C} = a_{\alpha\beta}\boldsymbol{A}^\alpha \otimes \boldsymbol{A}^\beta$ is the right Cauchy–Green tensor and $J_s = det(\boldsymbol{F}_s) = \lambda_1\lambda_2$ is the Jacobian expressing the areal dilatation. Assuming the two-dimensional hyperelastic membrane, the membrane tension $\boldsymbol{T}_s$ can be described by using a strain energy function $w_s(I_1, I_2)$ in the reference state, as

$$\boldsymbol{T}_s = \frac{1}{J_s}\boldsymbol{F}_s \cdot \frac{\partial w_s}{\partial \boldsymbol{E}_s} \cdot \boldsymbol{F}_s^T. \tag{2.14}$$

Using the chain rule, the expression for the contravariant representation of $\boldsymbol{T}_s$ is obtained as

$$T_s^{\alpha\beta} = \left[\frac{2}{J_s}\frac{\partial w_s}{\partial I_1}G^{\alpha\beta} + 2J_s\frac{\partial w_s}{\partial I_2}a^{\alpha\beta}\right]\boldsymbol{a}_\alpha \otimes \boldsymbol{a}_\beta. \tag{2.15}$$

This study has employed the constitutive law derived by Skalak *et al.* (1973) to express the behaviour of a biological membrane

$$w_s = \frac{G_s}{4}\left(I_1^2 + 2I_1 - 2I_2 + CI_2^2\right), \tag{2.16}$$

where G_s is surface shear elastic modulus and C is a non-dimensional parameter determining the areal incompressibility. In this work, the value of C was set to ten with reference to the erythrocyte model (Omori *et al.* 2013), which characterises strain hardening behaviour and the incompressible areal dilatation of the membrane. The Poisson ratio of the Skalak law is $\nu_s = C/(1 + C)$.

The bending energy of the membrane w_b is calculated based on a model proposed by Helfrich (1973)

$$w_b = \frac{E_b}{2}\int (2H - c_0)\,\mathrm{d}A, \tag{2.17}$$

https://doi.org/10.1017/jfm.2026.11965 Published online by Cambridge University Press

where H is a mean curvature of the membrane, c_0 is the spontaneous curvature and E_b is the bending modulus. By assuming a symmetric membrane property, (i.e. $c_0 = 0$), the bending energy can be converted to the load due to a bending $\boldsymbol{q}_b$ as (Matsui *et al.* 2020*a*)

$$\boldsymbol{q}_b = -2E_b\big[\Delta_s H + 2H(H^2 - K)\big]\boldsymbol{n}, \tag{2.18}$$

where Δ_s is the Laplace–Beltrami operator and K is the Gaussian curvature on the membrane surface.

2.3. *Fluid mechanics*

Considering the typical small size of swimming microorganisms, the surrounding flow field can be regarded as a Stokes flow. Thus, inertial effects on the internal and external flow fields can be neglected. The fluid velocity $\boldsymbol{v}$ at an arbitrary position $\boldsymbol{y}$ produced by N swimmers in an ambient flow $\boldsymbol{v}_\infty$ can be written as a boundary integral on the deformed membrane A and torque surface A_t (Pozrikidis 1992)

$$\boldsymbol{v}(\boldsymbol{y}) = \boldsymbol{v}_\infty(\boldsymbol{y}) - \frac{1}{8\pi\mu}\sum_i^N \left[\int_A \boldsymbol{J}(\boldsymbol{x},\boldsymbol{y})\cdot\boldsymbol{q}(\boldsymbol{x})\mathrm{d}A^i + \int_{A_t} \boldsymbol{R}(\boldsymbol{x},\boldsymbol{y})\cdot\boldsymbol{L}(\boldsymbol{x})\mathrm{d}A_t^i\right], \tag{2.19}$$

where μ is viscosity inside and outside the membrane. The ambient flow is imposed as a shear flow in the x–z plane with a shear rate $\dot{\gamma}$, given by $\boldsymbol{v}_\infty = (\dot{\gamma}z, 0, 0)$, in this work. The Green's functions $\boldsymbol{J}$ and $\boldsymbol{R}$ correspond to the stokeslet and rotlet in a triply periodic lattice, respectively (Beenakker 1986).

2.4. *Numerical method*

This section provides briefly discretisation of the soft swimmer and the numerical method combining membrane mechanics and fluid mechanics in the Stokes flow. The swimmer's membrane and torque surface are respectively discretised by 1280 triangular elements with 642 node points, as shown in figure 1(*a*). Local membrane deformations are tracked over time in the Lagrangian frame using these node points over time.

In order to solve the fluid–structure interaction between the membrane and surrounding fluid in the Stokes regime, this study has employed a numerical method similar to the previous work (Walter *et al.* 2010). For the membrane mechanics, there is an equilibrium relation between the load due to a membrane in-plane stretch $\boldsymbol{q}_s$ and membrane tension, which can be written in weak form based on the principle of virtual work as

$$\int_A \hat{\boldsymbol{u}}\cdot\boldsymbol{q}_s\mathrm{d}A = \int_A \hat{\boldsymbol{\varepsilon}} : \boldsymbol{T}\mathrm{d}A, \tag{2.20}$$

where $\hat{\boldsymbol{u}}$ and $\hat{\boldsymbol{\varepsilon}} = (1/2)(\nabla_s\hat{\boldsymbol{u}} + \nabla_s\hat{\boldsymbol{u}}^T)$ are a virtual displacement and strain, respectively. This equilibrium equation is solved numerically by using a finite-element method to obtain $\boldsymbol{q}_s$ from membrane tension defined geometrically according to the Skalak constitutive law. The viscous load $\boldsymbol{q}$ on the membrane is given by a superposition of loads due to the stretch and bending (i.e. $\boldsymbol{q} = \boldsymbol{q}_s + \boldsymbol{q}_b$). For the fluid mechanics of the surrounding flow, substituting $\boldsymbol{q}$ into the boundary integral equation (2.19) results in a new velocity field $\boldsymbol{v}$, which was calculated by a boundary-element method. This study has used a Gaussian quadrature method with six numerical integration points in each element to compute $\boldsymbol{v}$. A material point on the torque surface is given by $\boldsymbol{x}_t = \boldsymbol{x} + \varepsilon\boldsymbol{n}(\boldsymbol{x})$, and the flow due to the torque $\boldsymbol{L}$ is calculated in the same integral manner. The material point on the torque surface is defined as the point located a distance ε away from the membrane in the normal direction and the flow induced by the torque L is calculated using the same integration

https://doi.org/10.1017/jfm.2026.11965 Published online by Cambridge University Press

method. Here, ε was set to $0.05a$, which corresponds to the half-length of the cilium. Assuming a no-slip boundary at the membrane, $\mathrm{d}\boldsymbol{x}/\mathrm{d}t = \boldsymbol{v}$, the material point $\boldsymbol{x}$ is updated by a second-order Runge–Kutta method. The above cycles are iteratively calculated to simulate hydrodynamic interactions in the suspension.

In order to accelerate the computational process, a multipole expansion technique (Pozrikidis 1992) has been employed, classifying interactions into short-, middle- and long-range regimes depending on the distance between swimmers' centres (Matsunaga *et al.* 2016). Further details and settings are described in the Supplementary material. Mesh overlaps between swimmer surfaces can lead to numerical instabilities when the swimmers come into close proximity. Thus, pairwise repulsive force is introduced as an exponential function (Brady & Bossis 1985; Ishikawa & Pedley 2007), defined as

$$\boldsymbol{F}_{rep}(\boldsymbol{r}_t) = \begin{cases} \alpha_1 \dfrac{\alpha_2 \exp(-\alpha_2 r_t)}{1-\exp(-\alpha_2 r_t)} \dfrac{\boldsymbol{r}_t}{|\boldsymbol{r}_t|} & (|\boldsymbol{r}_t| \le a) \\ \boldsymbol{0} & (|\boldsymbol{r}_t| > a) \end{cases}, \tag{2.21}$$

where $\boldsymbol{r}_t$ is the distance between node points on the torque surface of each swimmer. The parameters related to the strength and decay rate of the repulsive force have been tuned as $\alpha_1 = 20$ and $\alpha_2 = 25$.

In this study, two non-dimensional parameters were introduced to characterise the system dynamics. The first is the capillary number, defined as

$$Ca = \frac{\mu U_0}{G_s}. \tag{2.22}$$

which quantifies membrane deformability as the ratio of viscous forces due to swimming with U_0 to the elastic restoring force of the membrane. The second parameter, $\dot{\gamma} a/U_0$, characterises the relative strength of the imposed shear flow compared with the swimmer's self-propulsion. All computations were normalised by using the swimmer's reference radius a, swimming speed U_0 and surface shear elastic modulus G_s.

2.5. *Rheological properties*

The particle bulk stress tensor can be obtained as the average of the stresslet over N particles in the unit domain

$$\boldsymbol{\Sigma}^{(p)} = \frac{1}{V}\sum_{i=1}^{N} \boldsymbol{S}_i = \frac{3c}{4\pi a^3} \langle \boldsymbol{S} \rangle , \tag{2.23}$$

where V is the volume of the unit fluid domain and $\langle\rangle$ means the ensemble average. This study focuses on the contributions to viscosity and normal stress differences as fundamental rheological properties of the suspension. The particle contribution to viscosity is given by

$$\frac{\mu_a - \mu}{\mu} = \frac{\Sigma_{xz}^{(p)}}{\dot{\gamma}\mu} = \frac{3c}{4\pi a^3 \dot{\gamma}\mu} \langle S_{xz} \rangle . \tag{2.24}$$

Here, μ_a is the apparent viscosity and $(\mu_a - \mu)/\mu$ is the specific viscosity. The dimensionless first and second normal stress differences are defined, in a similar manner, as

$$\frac{\Sigma_{xx}^{(p)} - \Sigma_{zz}^{(p)}}{\dot{\gamma}\mu} = \frac{3c}{4\pi a^3 \dot{\gamma}\mu} \langle S_{xx} - S_{zz} \rangle \tag{2.25}$$

https://doi.org/10.1017/jfm.2026.11965 Published online by Cambridge University Press

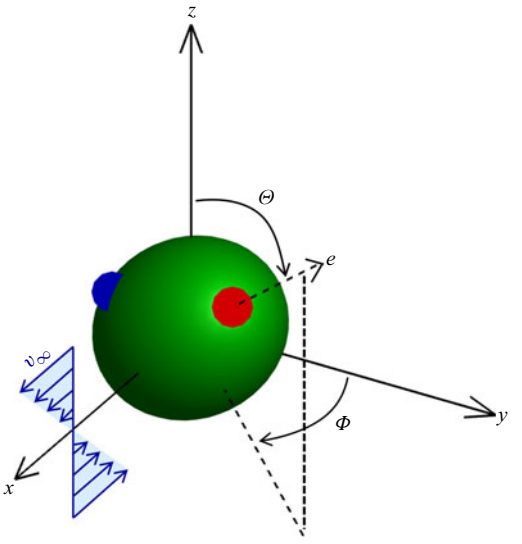


Figure 3. Problem setting of a simulation using the solitary swimmer model. The ellipsoidal swimmer with $AR = 2$ is initially oriented towards $\Phi = \Theta = \pi/4$. A shear flow is set in the x–z plane as $\boldsymbol{v}_\infty = (\dot{\gamma} z, 0, 0)$. A red (blue) marker shows the anterior (lateral) node point on the membrane.

and

$$\frac{\Sigma_{zz}^{(p)} - \Sigma_{yy}^{(p)}}{\dot{\gamma}\mu} = \frac{3c}{4\pi a^3 \dot{\gamma}\mu} \left\langle S_{zz} - S_{yy} \right\rangle. \tag{2.26}$$

3. Rheology in the dilute limit; without hydrodynamic interactions

We investigate shear viscosity and normal stress differences of the dilute suspension of soft microswimmers. According to the scaling of Batchelor & Green (1972), the rheological properties of the dilute suspension are described by the leading-order term of $O(c)$ in the polynomial expansion with respect to the volume fraction c, which is determined by the averaged hydrodynamic response of the solitary particle. Thus, the analysis of the dilute limit provides essential insight into the fundamental role of swimmer's deformability in their suspension rheology.

3.1. *Problem setting*

The ellipsoidal swimmer with $AR = 2$ was initially aligned with a polar angle of $\Theta = \pi/4$ and azimuthal angle of $\Phi = \pi/4$, as shown in figure 3. The capillary number Ca was fixed at 0.1 while the imposed shear rate was varied in each condition.

3.2. *Second normal stress difference*

A characteristic of the swimming behaviour of elliptical capsule swimmers in shear flows is the reorientation of their swimming direction, which differs from the Jeffery orbit. For example, swimming direction, which was initially oriented at $\Phi = \pi/4$, converges towards the vorticity direction ($\Phi = 0$) whilst undergoing rotation due to shear. Once convergence has occurred in the vorticity direction, the swimmer achieves steady motion even under shear flow. The reorientation of the elliptical capsule swimmer towards the vorticity direction produces significant differences between the pusher and puller with

https://doi.org/10.1017/jfm.2026.11965 Published online by Cambridge University Press

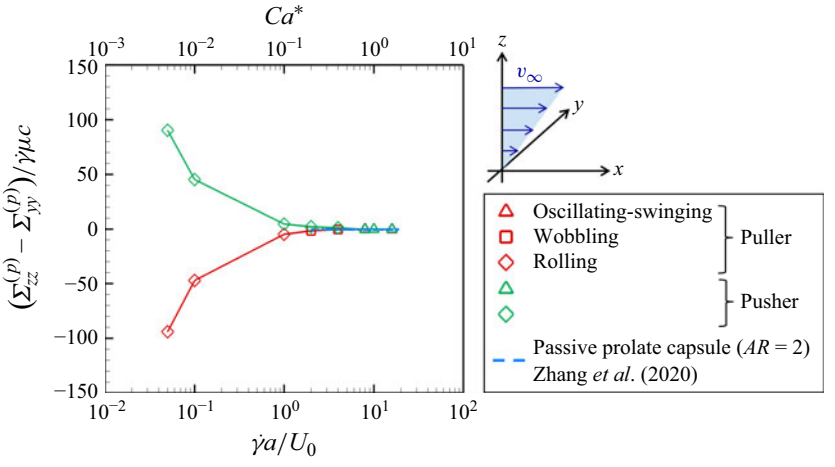


Figure 4. Second normal stress differences of the dilute suspensions estimated by the solitary swimmer with $AR = 2$ and $Ca = 0.1$. The values are averaged over one rotational period. Each marker shows the difference in the rotational mode in the steady motion. For comparison, a blue dashed lines indicate the results for a passive prolate capsule with $AR = 2$ (Zhang & Graham 2020). Here, Ca^* is the capillary number based on the shear flow defined as $Ca^* = \mu\dot{\gamma}/G_s$.

respect to the second normal stress difference. Thus, in this section, we mainly discuss the second normal stress difference of the suspension. For further details on the results regarding reorientation, shear viscosity and first normal stress difference are provided in the Supplemental Material.

We evaluated the second normal stress difference of the dilute suspension from the stresslet acting on the solitary swimmer during steady rotational motion. In the dilute limit, the suspension rheology is often discussed by evaluating the coefficient of the first-order term in the polynomial expansion with respect to c: the value of (2.26) divided by c. The result is shown in figure 4, where all data were averaged over the time for one rotation. In order to compare with the former results of ellipsoidal passive capsules, instead of microswimmers, we introduce another capillary number, Ca^*, defined using the viscous force due to the shear flow (Zhang & Graham 2020)

$$Ca^* = \frac{\mu\dot{\gamma}a}{G_s}. \tag{3.1}$$

Due to the deformability, the swimmer tends to reorient in its rotational motion. As a result, the second normal stress difference shows a different tendency depending on the swimming mode, especially in the low shear rate regime. At low shear rates, the swimming directions of both the pusher and the puller are aligned with the vorticity direction. Even when the swimming directions are the same, the stresslet in the orientational and lateral directions is opposite for pushers and pullers. Thus, the second normal stress difference yields markedly different results for the pusher and puller. Conversely, at the high shear rates ($Ca^* > 0.5$), this stress difference asymptotically approaches that of the passive capsule regardless of the swimming mode because the swimmer deforms mainly due to the background flow.

https://doi.org/10.1017/jfm.2026.11965 Published online by Cambridge University Press

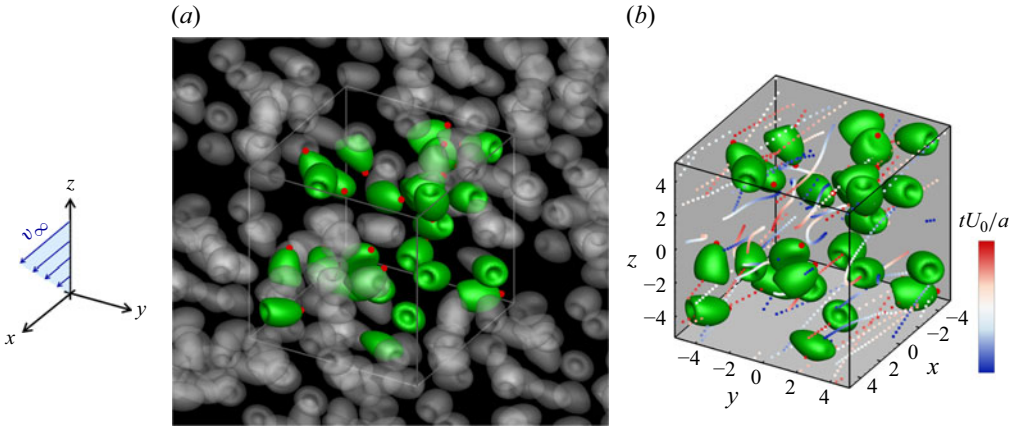


Figure 5. Problem setting of a simulation using multiple swimmer models. (*a*) Twenty-seven swimmers are suspended in the computational unit, and the triply periodic boundary condition is applied to the domain. The shear flow is set in the x–z plane as $\boldsymbol{v}_\infty = (\dot{\gamma} z, 0, 0)$. (*b*) Instantaneous snapshot of 27 pusher swimmers in the sheared suspension ($c = 0.1$). Red and blue square markers show trajectories of the swimmers.

4. Active rheology due to hydrodynamics interactions

In the semi-dilute regime, two- and three-body interactions begin to emerge and significantly affect the microstructure and suspension rheology. In order to account for their hydrodynamic interactions, we developed the mono-dispersed suspension model, as described in (2.19). This section provides a detailed analysis of how these interactions influence the orientational distribution and the resulting macroscopic rheological properties, with particular attention to the effects of the swimmer's membrane stiffness and body shape.

4.1. *Problem setting*

We applied triply periodic boundary conditions proposed by Lees & Edwards (1972) to the computational cubic lattice, to express hydrodynamic interactions in the infinite domain. Initially, twenty-seven swimmers were randomly assigned positions and orientations within the domain, as shown in figure 5(*a*). By adjusting the size of the domain, the desired volume fraction c can be controlled. The shear flow was set in the x–z plane as $\boldsymbol{v}_\infty = (\dot{\gamma} z, 0, 0)$ (cf. figure 5*b*).

4.2. *Distribution of swimmers' orientations*

First, we investigate how the orientation of microswimmers changes in a more concentrated suspension, where interactions between the swimmers cannot be ignored. We define the orientational correlation function I_v between the swimmer's orientation and the vorticity axis as follows:

$$I_v = \frac{3}{2}\left\langle (\boldsymbol{e}_i \cdot \boldsymbol{n}_v)^2 - \frac{1}{3} \right\rangle_N, \tag{4.1}$$

where $\boldsymbol{n}_v$ is the vorticity axis: $\boldsymbol{n}_v = (0, 1, 0)$. Specifically, $I_v = 1$ corresponds to the swimmer being parallel to $\boldsymbol{n}_v$, $I_v = -0.5$ corresponds to a perpendicular orientation and $I_v = 0$ indicates an isotropic distribution with respect to $\boldsymbol{n}_v$. Typical results of ellipsoidal pushers and pullers with $AR = 2$ are shown in figures 6(*a*) and 6(*b*), respectively. The shear strength is set as $\dot{\gamma} a/U_0 = 0.05$ and the capillary number is 0.1 for both cases.

https://doi.org/10.1017/jfm.2026.11965 Published online by Cambridge University Press

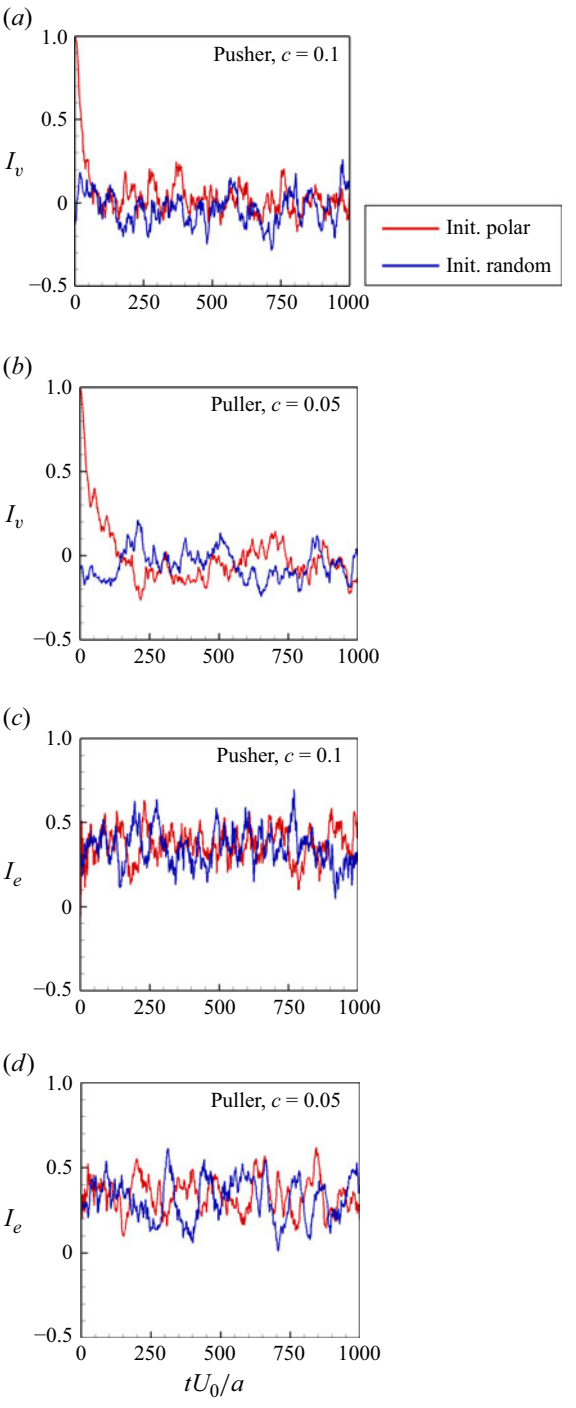


Figure 6. (*a–b*) Time evolution of the correlation function between the swimmer's orientation and vorticity axis of the shear flow in the suspension. (*c–d*) Time evolution of the correlation function between the projected swimmer's orientation in the shear plane and elongational axis of the shear flow. The swimmers with $AR = 2$ and $Ca = 0.1$ are exposed to the shear flow with $\dot{\gamma}a/U_0 = 0.05$.

https://doi.org/10.1017/jfm.2026.11965 Published online by Cambridge University Press

The correlation function reached a developed state when $tU_0/a > 250$ for both swimmer types. In the case of the dilute limit without the cell–cell interactions, the swimmer in low shear rate tends to align to the vorticity axis of the shear flow (cf. Supplementary Material). However, when the interparticle interaction is considered, the time-averaged value in the developed state converges to nearly zero. This result suggests that reorientation towards the vorticity direction is being eliminated by fluid interactions between swimmers. Furthermore, to verify initial condition dependence, the simulations were initiated from a polar-order state where the initial swimming direction was aligned with the vorticity axis. Even in this case, it was confirmed that the value of the correlation function finally approaches zero. These results suggest that hydrodynamic interactions prevent the reorientation of microswimmers along the vorticity axis.

The question arises as to whether the swimmer is swimming isotropically within three-dimensional space. We subsequently define an additional correlation function, I_e, in a manner analogous to (4.1). By changing the reference axis from $\boldsymbol{n}_v$ to the extension direction vector $\boldsymbol{n}_e = (1/\sqrt{2}, 0, 1/\sqrt{2})$, we obtain a quantity I_e that represents the correlation between the projected swimmer's orientation and elongational axis of the shear flow. As shown in figures 6(*c*) and 6(*d*), the value of I_e is positive and no longer equal to zero. This suggests that the mean swimming directions manifest an asymmetric distribution, exhibiting a bias towards the direction of shear elongation.

In order to gain deeper insight into these results, we evaluate the averaged orientational distribution of the swimmers using the generalised orientation distribution function P, defined as

$$P = \frac{\langle N_l(\Phi, \Theta)\rangle_t}{\Delta S(\Delta\Phi, \Delta\Theta) n_{mean}}, \tag{4.2}$$

where N_l is defined by the number of swimmers oriented within the surface element ΔS on the unit sphere defined by angular intervals of $\Delta\Phi$ and $\Delta\Theta$, and $n_{mean} = N/4\pi$ is the global surface number density. Figure 7(*a–d*) shows contour plots of P mapped onto the spherical surface. An anisotropic distribution concentrated in the elongational direction is observed at low shear rates $\dot{\gamma}a/U_0 = 0.05$. As the shear strength increases, the orientational distribution becomes biased towards the streamwise direction. At very high levels of shear, the distribution concentrates on the shear plane. Such shear plane concentrations can be attributed to the predominance of external flow, which, in conjunction with the vorticity inherent in the shear flow, results in an augmentation of swimmer's rotation. These results indicate that the orientational distribution in the low shear regime becomes more asymmetric with the bias in the elongational quadrant. Changes in the swimming direction due to fluid interactions exert an effective randomness analogous to thermal fluctuations in Saintillan (2010). In the rotation of rod-like objects within a shear flow field, orientational fluctuations lead to symmetry breaking between the times spent in the extensional and compressional quadrants. This effect becomes dominant in the low shear rate regime because the time scale required for alignment due to the interactions is likely shorter than that for flow-induced reorientation towards the vorticity axis. Although hydrodynamic interaction also induces local swimmers' aggregation and weak nematic order in the near field, these effects are not strong enough to form a global coherent polar order.

4.3. *Shear viscosity and normal stress differences*

Based on the results shown in figure 6, this study evaluated the rheological properties of the suspension of the soft microswimmers as time-averaged values over one rotational period after the microstructure had reached a sufficiently developed steady state.

https://doi.org/10.1017/jfm.2026.11965 Published online by Cambridge University Press

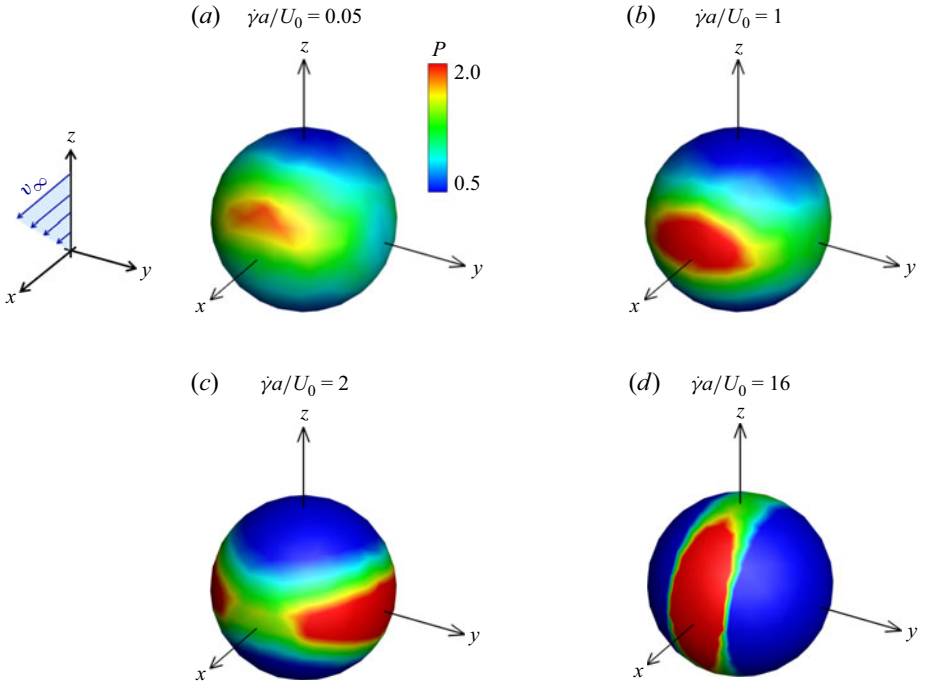


Figure 7. (*a–d*) Orientational distribution for pusher suspensions with $AR = 2$, $Ca = 0.1$, $c = 0.1$ and various $\dot{\gamma}a/U_0$. Here, $P(\Theta, \Phi)$ is defined as the time-averaged probability density of the orientation over one rotational period, which has been normalised by the homogeneous one.

Results of the pusher suspensions with $Ca = 0.1$ are shown in figure 8. Similar to the former experiments (Rafaï *et al.* 2010; López *et al.* 2015), negative specific viscosity was measured when $\dot{\gamma}a/U_0 \sim 0.1$ and the value decreases with higher c (see figure 8*a*). In contrast, for high $\dot{\gamma}a/U_0$, the results show the shear-thinning characteristic with positive values. Regarding the normal stress differences of the pusher suspension, the response to shear differs qualitatively between the first and second normal stress differences (cf. figures 8*b* and 8*c*). The first normal stress differences in the pusher suspension become negative in low shear rate regimes, because the pusher swimmer orienting closer to the streamwise direction generates a negative active stress $\Sigma^{(p)}_{xx}$. In the transverse direction, on the other hand, it tends to generate a positive active stress, meaning that the first normal stress difference tends to be negative. In the vorticity axis direction, the orientational distribution is isotropic. In the shear plane, however, the swimming direction is slightly offset from the streamwise direction towards the extensional direction. Consequently, a difference arises between $\Sigma^{(p)}_{zz}$ and $\Sigma^{(p)}_{yy}$, generating a positive second normal stress difference. By contrast, at high shear rates, shear-induced deformation becomes more dominant than that of propulsive torque, as the swimmers are stretched primarily in the x-direction and compressed in the y- and z-directions by the shear flow. Therefore, under high shear, the first normal stress difference becomes positive while the second normal stress difference asymptotically approaches zero.

Next, we investigate the rheology of the puller suspensions. The capillary number is again set as $Ca = 0.1$ and the result is shown in figure 9. Basically, the orientational distributions of pullers are similar to those of the pusher suspensions. However, the sign

https://doi.org/10.1017/jfm.2026.11965 Published online by Cambridge University Press

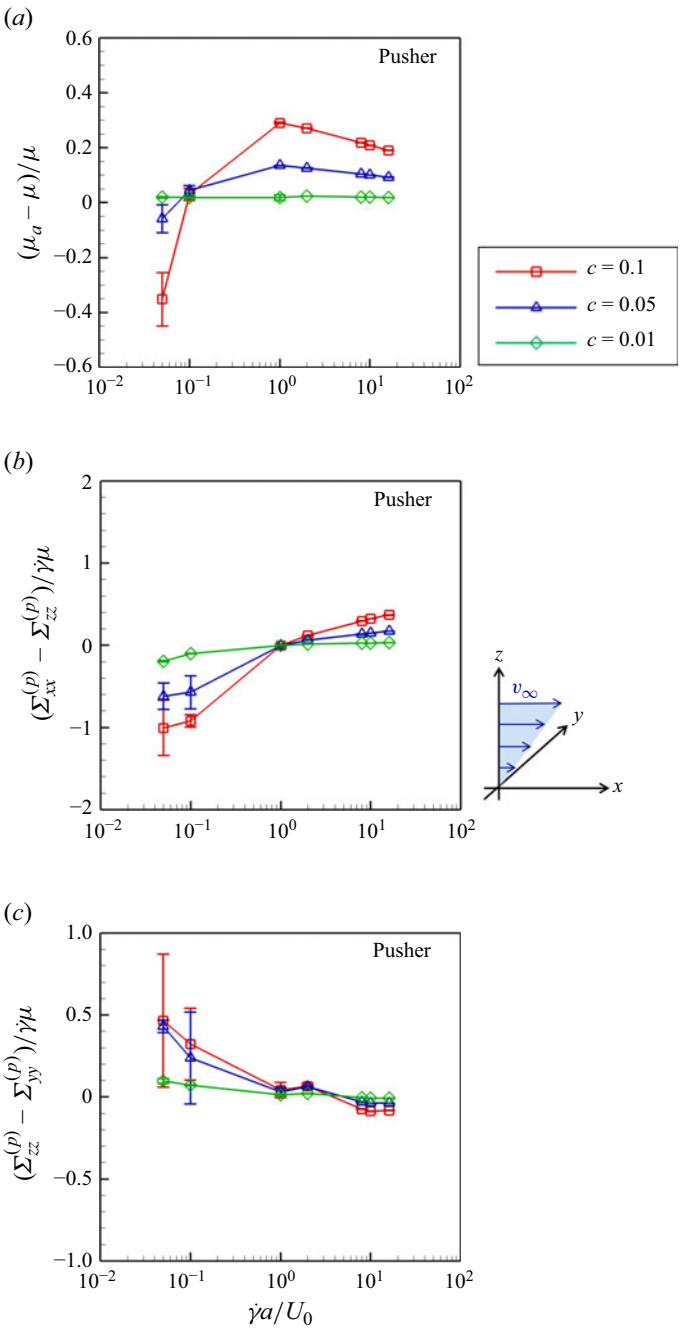


Figure 8. Rheological properties of suspensions of pusher swimmers with $AR = 2$ and $Ca = 0.1$. (*a*) Specific viscosity. The contributions to (*b*) 1st and (*c*) 2nd normal stress differences. Error bars mean standard deviations for the three independent cases discussed throughout the paper.

https://doi.org/10.1017/jfm.2026.11965 Published online by Cambridge University Press

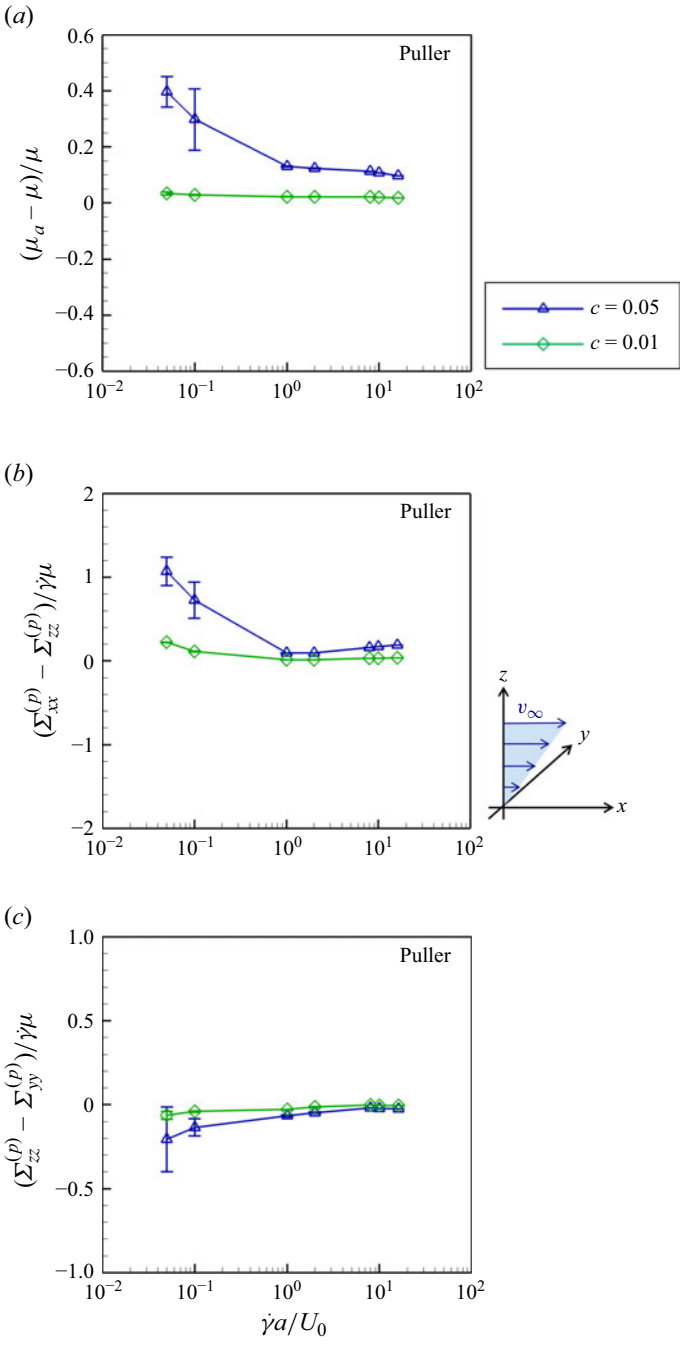


Figure 9. Rheological properties of suspensions of puller swimmers with $AR = 2$ and $Ca = 0.1$. (*a*) Specific viscosity. The contributions to (*b*) 1st and (*c*) 2nd normal stress differences.

of the active stress generated by the puller is opposite to that of the pusher. Therefore, at low shear rates, the puller exhibits a high viscosity increase (cf. figure 9*a*). This effect is observed at a volume fraction of around 0.05 and is barely noticeable at a volume fraction of 0.01, where the frequency of interactions also decreases. Similarly, the results for normal

https://doi.org/10.1017/jfm.2026.11965 Published online by Cambridge University Press

stress differences are the opposite of those for pushers. At low shear rates, the first normal stress difference is positive, while the second is negative.

4.4. *Specific viscosity in dilute suspensions with or without hydrodynamic interactions*

According to the scaling by Batchelor & Green (1972), the frequency of n-body interaction is proportional to c^n. For $c = 0.01$, the contribution of two-body interactions is expected to be approximately 1 % of that of a solitary swimmer. Thus, the rheological properties of the suspension with $c = 0.01$ can be expected to be well described by the leading-order term of $O(c)$ in this scaling. However, the comparison between the multi-body system and solitary swimmer reveals distinct differences arising from alignment of the swimmers at the low shear rate (cf. figure 10). When the hydrodynamic interactions between swimmers are considered, the viscosity contribution of the pusher decreases relative to the results of the solitary swimmer, and *vice versa* for the puller. These results demonstrate that interactions between swimmers play a decisive role in disrupting stable orbital motion in shear flow, even at a volume fraction of 1 % and with a low frequency of hydrodynamic interactions. In other words, the ideal approximation of the active suspension rheology based on the solitary motion might be untenable, even in low volume fractions. Indeed, the previous experiments (Rafaï *et al.* 2010; López *et al.* 2015) reported inherent viscosity change at the low volume fraction with the range of $O(10^{-3})$. It is expected that hydrodynamic interactions will be effective because the presence of flagella enables cells to interact over a wider range.

4.5. *Comparison with hydrodynamic interactions and Brownian rotational diffusion*

From the discussion so far, we found that the interparticle hydrodynamic interaction induces effective orientational fluctuation and results in a biased distribution towards the elongational direction of the shear flow. Similar distributions have been reported by Saintillan (2010) using a time-dependent Fokker–Planck equation for orientation. In this model, orientational fluctuations are modelled as Brownian diffusion. Here, clarifying the differences between fluctuations arising from hydrodynamic interactions and those due to Brownian rotational diffusion may be worthwhile. In order to consider the effects of Brownian motion on the suspension rheology, we added Gaussian noise to the rotational motion of the soft swimmer. Assuming isotropic diffusivity, the rotational displacement due to the Brownian motion $\Delta\omega_b$ follows a Gaussian distribution with $\langle \Delta\omega_b(\Delta t)\rangle = 0$ and is defined by D_R as

$$\Delta\omega_b(\Delta t) = \sqrt{2D_R\Delta t}. \tag{4.3}$$

Here, the non-dimensional rotational diffusivity is set as $D_R^* = D_R a/U_0 = 0.004$ as estimated from the simulation results of a non-Brownian soft swimmer for a volume fraction of $c = 0.1$, without background flow ($\dot{\gamma}a/U_0 = 0$), a capillary number of $Ca = 0.1$ and an aspect ratio of $AR = 2$. The results of the Brownian soft swimmer are shown in figure 11. Similar to hydrodynamic interactions, a biased orientational distribution towards elongation was observed even in the solitary Brownian soft pusher at the low shear rate $\dot{\gamma}a/U_0 = 0.05$. However, the higher peak value of P on the line of $\Phi = 0.5\pi$ for the Brownian swimmer is observed, compared with the result considering only the fluctuation induced by the interparticle hydrodynamic interaction. This quantitative discrepancy is likely attributable to the emergence of a weak alignment effect arising from the hydrodynamic interaction. As a result, the degree of specific viscosity becomes higher (cf. figure 11*c*). These results imply that the effects of hydrodynamic interactions on suspension rheology cannot be fully replaced by those of Brownian noise.

https://doi.org/10.1017/jfm.2026.11965 Published online by Cambridge University Press

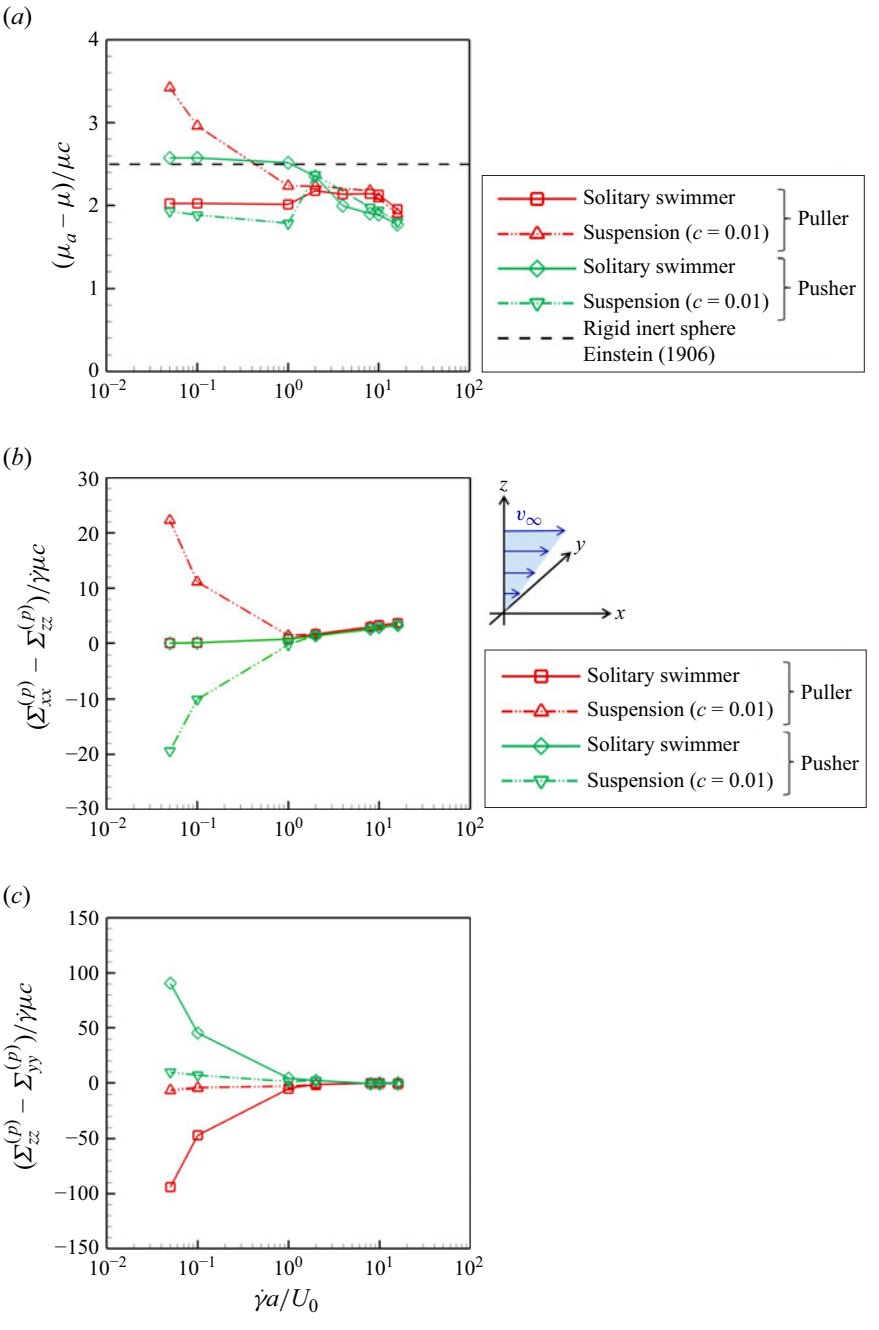


Figure 10. Comparison of the rheological properties in the dilute regime obtained by multiple swimmer models with $c = 0.01$, with those estimated by the solitary swimmer model. (*a*) Viscosity contribution. The (*c*) 1st and (*d*) 2nd normal stress differences. The aspect ratio of the swimmer is set to 2 and capillary number is set to 0.1.

https://doi.org/10.1017/jfm.2026.11965 Published online by Cambridge University Press

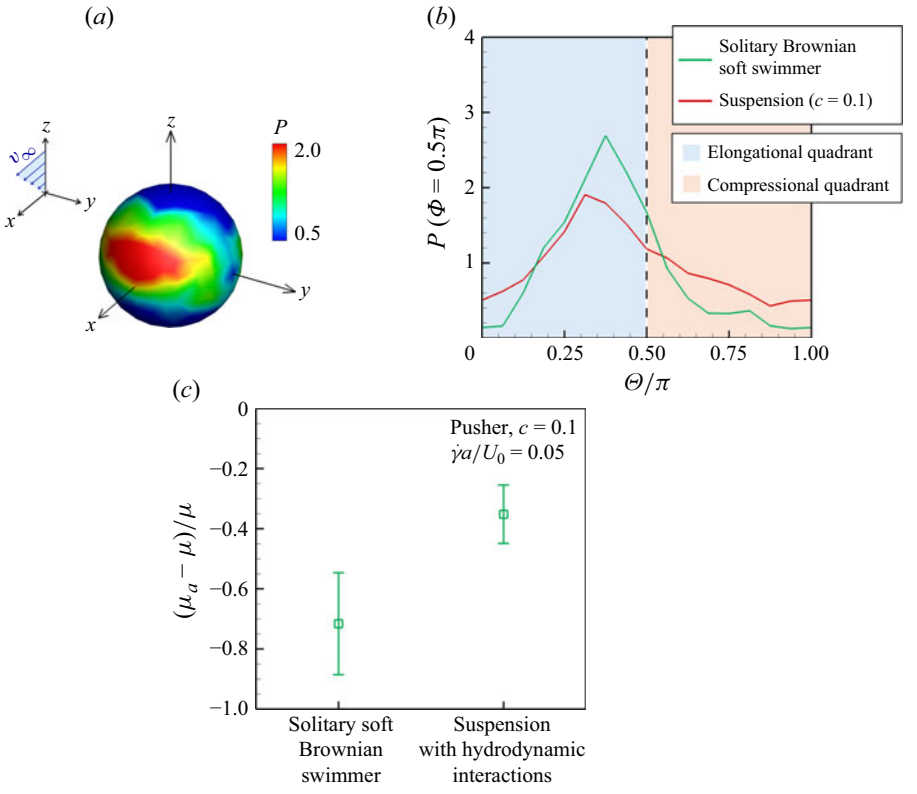


Figure 11. (*a*) Orientational distribution estimated by the solitary Brownian soft pusher. (*b*) Distribution of $P(\Theta)$ in the shear plane ($\Phi = 0.5\pi$). The red line indicates the results of non-Brownian soft pushers with hydrodynamic interactions, whilst the green line represents the results of a solitary Brownian soft pusher. (*c*) Specific viscosity estimated from a solitary Brownian soft pusher and non-Brownian soft pushers with hydrodynamic interactions. The results for Brownian swimmer assume a dilute limit ($\mu_a \sim \mu - 7.16c$) and, for comparison, have been estimated using a volume fraction of $c = 0.1$.

4.6. *Effects of the capillary number*

In this section, we investigate the effects of Ca on specific viscosity and normal stress differences. The shear rate is set as $\dot{\gamma}a/U_0 = 0.05$ for all cases. The change in Ca under a fixed value of $a\dot{\gamma}/U_0$ is similar to the change in membrane stiffness.

The orientational distributions of the swimmers for various Ca are shown in figure 12. Due to numerical instability arising from excessive membrane deformation, stable simulations in this study were limited to pusher suspensions with $Ca \geq 0.1$ and puller suspensions with $Ca \leq 0.1$, respectively. In the pusher suspensions, the increase in Ca resulted in the decrease in the peak value of P. Consequently, as Ca increases, the effect of active stress approaches zero (see figure 13). On the other hand, Ca has little influence on the normal stress differences. For pullers, the peak value of P does not change with Ca, but Θ at which P is the maximum shifts slightly closer to the x-axis ($\Theta = 0.5\pi$) as Ca increases. As the bias in the direction of elongation is reduced, the effect of active stress diminishes with increasing Ca, much like with the pusher.

These results suggest that membrane deformability influences primarily viscosity through structural changes in the orientational distribution of swimmers. In particular, we infer that a softer membrane reduces the contribution of active stress to shear viscosity.

https://doi.org/10.1017/jfm.2026.11965 Published online by Cambridge University Press

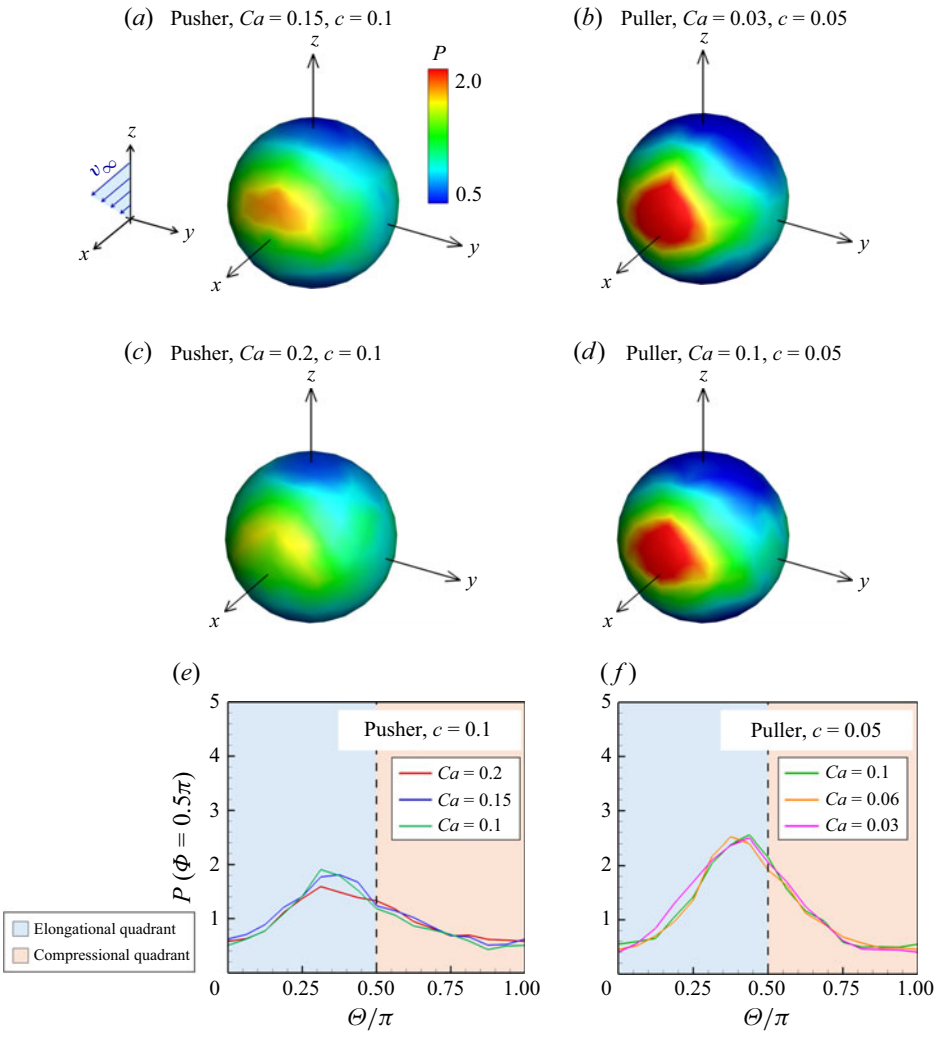


Figure 12. Effects of Ca on the orientational distribution of the swimmers. The left (right) graphs indicate results of pusher suspensions with $c = 0.1$ (puller suspensions with $c = 0.05$) and $\dot{\gamma}a/U_0 = 0.05$. The aspect ratio of the swimmer is set to 2: (*a*) $Ca = 0.15$ and (*c*) $Ca = 0.2$ of pusher swimmers; (*b*) $Ca = 0.03$ and (*d*) $Ca = 0.1$ of puller swimmers. (*e–f*) Orientation distribution functions on the line with $\Phi = 0.5\pi$. The blue (red) area indicates that the swimmer spends in the extensional (compressional) quadrant.

4.7. *Effects of the aspect ratio*

Finally, we investigate the effects of the aspect ratio AR on the suspension rheology. The capillary number and shear rate are set to 0.1 and 0.05, respectively. For $AR = 1$, the resultant orientation distribution is almost isotropic for both pushers and pullers, as shown in figure 14. Generally, the soft spherical swimmer rotates at an almost constant angular velocity during the one-periodic rotation (Matsui *et al.* 2020*b*). By contrast, ellipsoidal swimmers, like Jeffery orbits, have a non-constant rotational speed and tend to spend more time aligned with the streamwise direction. As the swimmer's aspect ratio increases, a bias towards an orientation in the direction of shear elongation becomes observable (see figures 14*b* and 14*c*), due to uneven rotational velocity and fluid interactions between particles.

https://doi.org/10.1017/jfm.2026.11965 Published online by Cambridge University Press

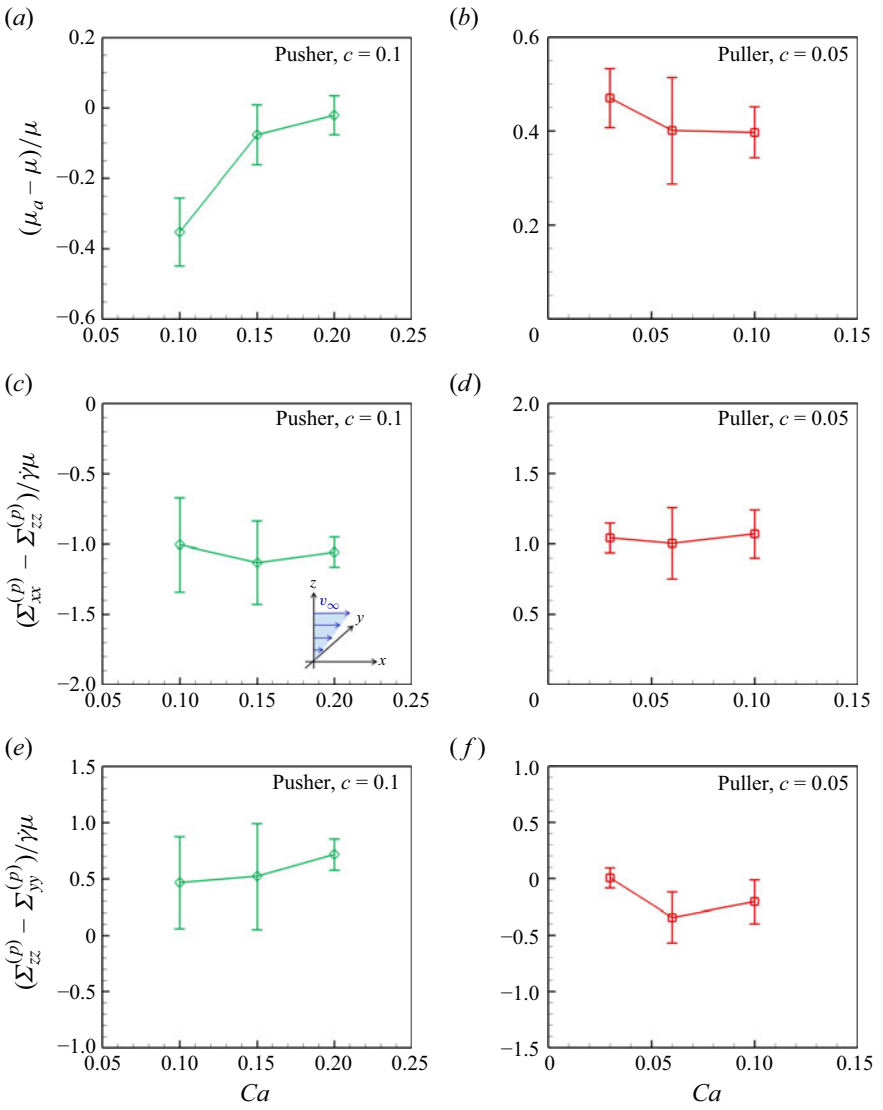


Figure 13. Effects of Ca on the rheological properties. (*a–b*) Specific viscosity. (*c–d*) Contribution to 1st normal stress differences. (*e–f*) Contribution to 2nd normal stress differences. The left (right) graphs indicate results of pusher suspensions with $c = 0.1$ (puller suspensions with $c = 0.05$) and $\dot{\gamma}a/U_0 = 0.05$. The aspect ratio of the swimmer is set to 2.

Changes in the aspect ratio also strongly influence rheology due to differences in orientation distribution (cf. figure 15). In pusher suspensions, specific viscosity changes from positive to negative values as the aspect ratio increases. In pullers, however, viscosity increases with the aspect ratio. For the first normal stress difference, the negative value increases with AR for the pusher, but increases monotonically for the puller. The second normal stress difference is similarly affected by the aspect ratio, with values increasing in the pusher and decreasing in the puller. These results suggest that the swimmer's body shape is one of the crucial factors causing the asymmetrical orientational distribution, resulting in the appearance of the active rheology of the microswimmers.

https://doi.org/10.1017/jfm.2026.11965 Published online by Cambridge University Press

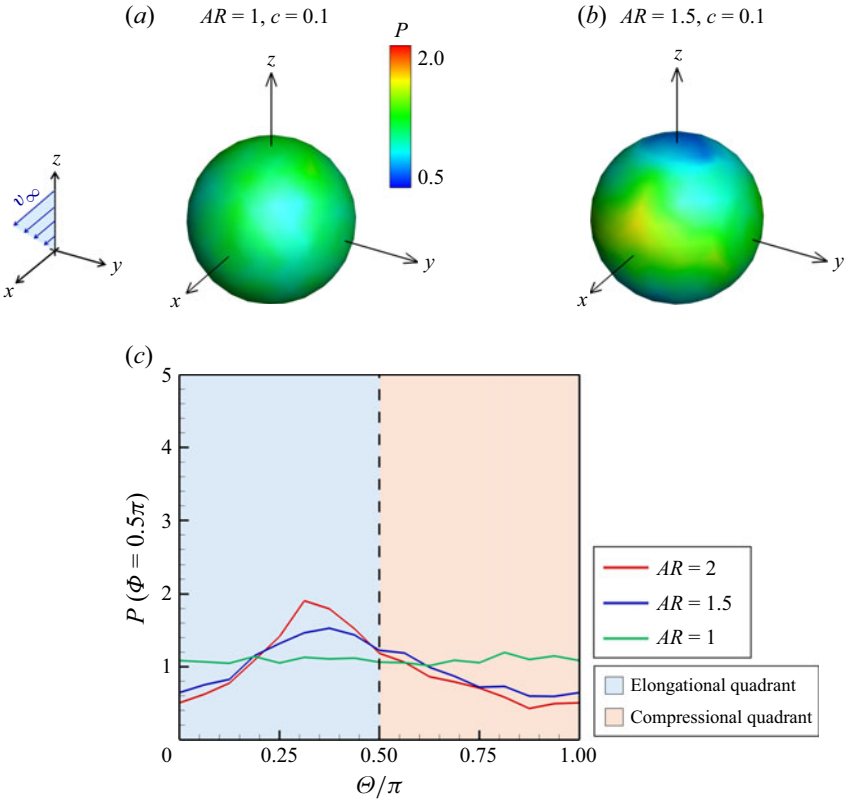


Figure 14. Effects of the swimmer's shape on the orientational distribution for the pusher suspensions with $c = 0.1$ and $\dot{\gamma}a/U_0 = 0.05$. The capillary number is set to 0.1: (*a*) $AR = 1$, (*b*) $AR = 1.5$. (*c*) Distribution of $P(\Theta)$ in the shear plane ($\Phi = 0.5\pi$).

5. Conclusion

In this study, we investigated the suspension rheology of deformable soft microswimmers based on their orientational behaviour. For the dilute regime, the swimmer in simple shear flow shows a reorientation due to membrane deformation during the rotational motion. Consequently, the contributions of the active stress to the second normal stress difference appear in the low shear rate regime, which produces the significant rheological difference between the pusher and puller suspensions. In contrast, in the high shear rate regime, the contributions to the rheological properties are determined by the large deformation of the swimmer due to the shear flow, so that the rheological difference between the swimmer types is reduced.

For the non-dilute regimes, it was revealed that the hydrodynamic interactions under low shear rates cause a transition of the swimmer's orientation towards the shear plane and perturbation of the stable rotational motion. This randomness due to hydrodynamic collisions leads to an orientational distribution biased towards the elongational direction of the shear flow during the swimmers' rotation, increasing the time spent in the elongational quadrant. As a result, specific viscosity and the first normal stress difference of the pusher (puller) suspension become negative (positive) signs. The second normal stress difference of the pusher (puller) suspension becomes a positive (negative) sign. This mechanism is analogous to the orientational decorrelation mechanism reported by Saintillan (2010), but this study demonstrated that only the hydrodynamic interactions are sufficient to

https://doi.org/10.1017/jfm.2026.11965 Published online by Cambridge University Press

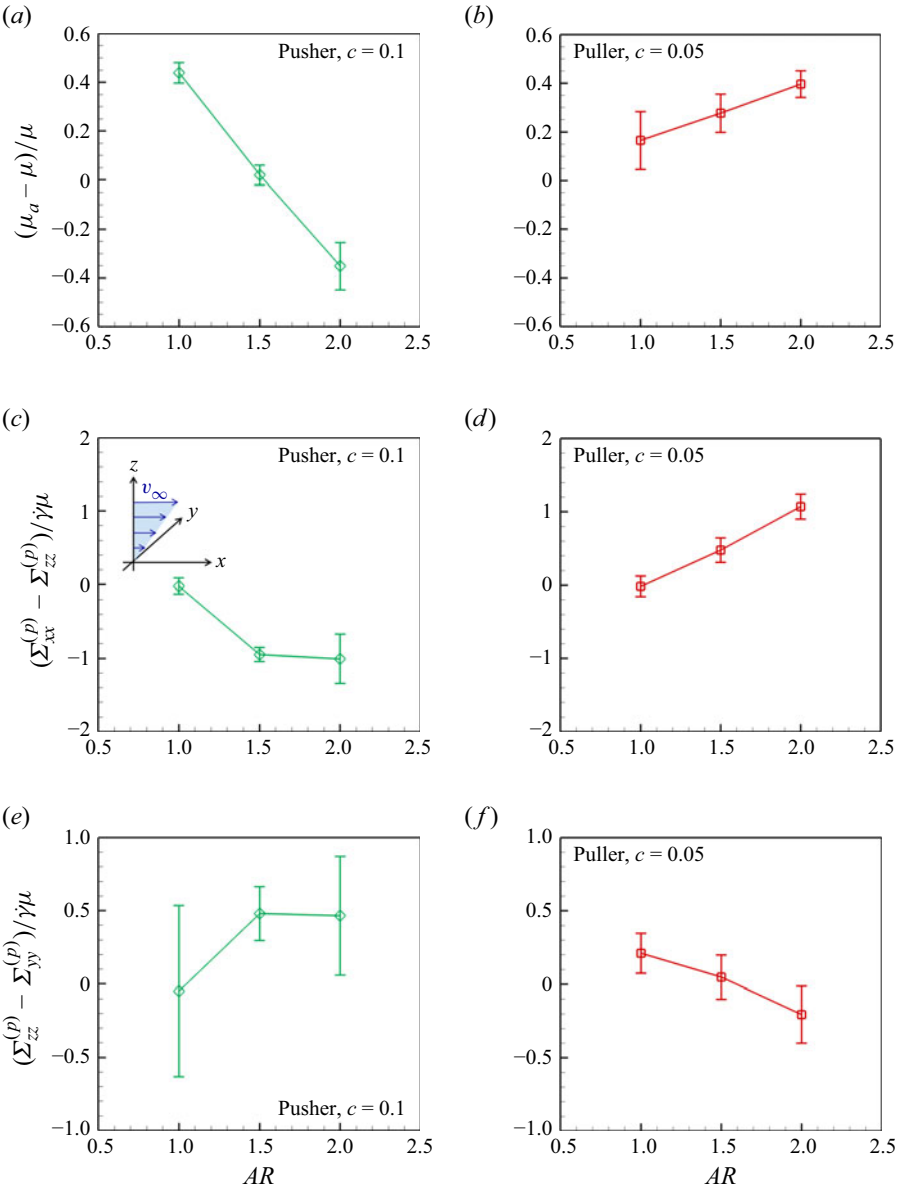


Figure 15. Effects of swimmers' shapes on the rheological properties. The capillary number is set to 0.1 in all swimmer and shear rate is set to 0.05. (*a*,*b*) Specific viscosity. (*c*,*d*) Contribution to 1st normal stress differences. (*e*,*f*) Contribution to 2nd normal stress differences. The left (right) graphs indicate results of pusher suspensions with $c = 0.1$ (puller suspensions with $c = 0.05$).

produce negative specific viscosity of the pusher suspension observed in the experiment (López *et al.* 2015). In addition, this study showed that the effect of fluctuation arising from hydrodynamic interactions cannot simply be replaced with that of Brownian motion.

We conducted a parametric study focusing on the shape matter and deformability of the swimmer. As a result, it was found that the swimmer's ellipsoidal shape is one of the influential factors leading to the biased orientational distribution in the elongational

https://doi.org/10.1017/jfm.2026.11965 Published online by Cambridge University Press

direction. Regarding the effects of the membrane stiffness, the softer swimmers weaken randomness induced by the interparticle collision because of membrane deformation. Consequently, the soft swimmers are less likely to form the biased structure, thereby weakening the contribution of the active stress to specific viscosity. The findings obtained in this study provide valuable insights and important indicators for predicting and controlling the flow behaviour of macroscopic suspensions of swimming microorganisms in natural environments.

Supplementary material. Supplementary material is available at https://doi.org/10.1017/jfm.2026.11965.

Funding. K.K. was supported by JSPS KAKENHI Grants No. JP25KJ0567. T.I. was supported by JST CREST Grant No. JPMJCR25Q1 and by JSPS KAKENHI Grants No. 21H04999, 21H05308 and 26H02595. T.O. was supported by JST PRESTO Grant No. J210002385 and by JSPS KAKENHI Grants No. 24H01458.

Declaration of interests. The authors report no conflict of interest.

References

Barthès-Biesel, D., Diaz, A. & Dhenin, E. 2002 Effect of constitutive laws for two-dimensional membranes on flow-induced capsule deformation. *J. Fluid Mech.* **460**, 211–222.

Batchelor, G.K. 1970 The stress system in a suspension of force-free particles. *J. Fluid Mech.* **41**, 545–570.

Batchelor, G.K. & Green, J.T. 1972 The determination of the bulk stress in a suspension of spherical particles to order c^2. *J. Fluid Mech.* **56**, 401–427.

Beenakker, C.W.J. 1986 Ewald sum of the Rotne–Prager tensor. *J. Chem. Phys.* **85** (3), 1581–1582.

Blake, J.R. 1971 A spherical envelope approach to ciliary propulsion. *J. Fluid Mech.* **46** (1), 199–208.

Bossis, G. & Brady, J.F. 1984 Dynamic simulation of sheared suspensions. I. General method. *J. Chem. Phys.* **80** (10), 5141–5154.

Brady, J.F. & Bossis, G. 1985 The rheology of concentrated suspensions of spheres in simple shear flow by numerical simulation. *J. Fluid Mech.* **155**, 105–129.

Brady, J.F. & Bossis, G. 1988 Stokesian dynamics. *Annu. Rev. Fluid Mech.* **20**, 111–157.

Brady, J.F. & Morris, J.F. 1997 Microstructure of strongly sheared suspensions and its impact on rheology and diffusion. *J. Fluid Mech.* **348**, 103–139.

Brenner, H. 1974 Rheology of a dilute suspension of axisymmetric Brownian particles. *Intl J. Multiphase Flow* **1** (2), 195–341.

Dupont, C., Salsac, A.-V. & Barthès-Biesel, D. 2013 Off-plane motion of a prolate capsule in shear flow. *J. Fluid Mech.* **721**, 180–198.

Einstein, A. 1906 Eine neue bestimmung der moleküldimensionen. *Ann. Phys.* **324**, 289–306.

Guazzelli, É. & Pouliquen, O. 2018 Rheology of dense granular suspensions. *J. Fluid Mech.* **892**, P1.

Guo, S., Samanta, D., Peng, Y., Xu, X. & Cheng, X. 2018 Symmetric shear banding and swarming vortices in bacterial superfluids. *Proc. Natl Acad. Sci. USA* **115** (28), 7212–7217.

Guzmán, M. & Soto, R. 2019 Nonideal rheology of semidilute bacterial suspensions. *Phys. Rev. E* **99**, 012613.

Hatwalne, Y., Ramaswamy, S., Rao, M. & Simha, R.A. 2004 Rheology of active-particle suspensions. *Phys. Rev. Lett.* **92**, 118101.

Helfrich, W. 1973 Elastic properties of lipid bilayers: theory and possible experiments. *Z. Naturforsch. C* **28**, 693–703.

Ishikawa, T. 2025 Transport phenomena in microswimmer suspensions: migration, collective motion, diffusion and rheology. *J. Fluid Mech.* **1016**, P1.

Ishikawa, T., Brumley, D.R. & Pedley, T.J. 2021 Rheology of a concentrated suspension of spherical squirmers: monolayer in simple shear flow. *J. Fluid Mech.* **914**, A26.

Ishikawa, T., Brumley, D.R. & Pedley, T.J. 2025 Poiseuille flow of a concentrated suspension of squirmers. *J. Fluid Mech.* **1003**, A23.

Ishikawa, T., Losei, J.T. & Pedley, T.J. 2008 Development of coherent structures in concentrated suspensions of swimming model micro-organisms. *J. Fluid Mech.* **615**, 401–431.

Ishikawa, T. & Pedley, T.J. 2007 The rheology of a semi-dilute suspension of swimming model micro-organisms. *J. Fluid Mech.* **588**, 399–435.

Ishikawa, T., Simmondos, M.P. & Pedley, T.J. 2006 Hydrodynamic interaction of two swimming model micro-organisms. *J. Fluid Mech.* **568**, 119–160.

https://doi.org/10.1017/jfm.2026.11965 Published online by Cambridge University Press

ISHIKAWA, T., TANAKA, T., IMAI, Y., OMORI, T. & MATSUNAGA, D. 2016 Deformation of a micro-torque swimmer. *Proc. R. Soc. Lond. A* **472** (2185), 20150604.

JEFFERY, G.B. 1922 The motion of ellipsoidal particles immersed in a viscous fluid. *Proc. R. Soc. Lond. A* **102** (715), 161–179.

JEFFREY, D.J. & ACRIVOS, A. 1976 The rheological properties of suspensions of rigid particles. *AIChE J.* **22** (3), 417–432.

KUBO, K., OMORI, T. & ISHIKAWA, T. 2025 Microstructure and deformation in suspensions of soft microswimmers. *J. Fluid Mech.* **1011**, A31.

LAC, E., BARTHES-BIESEL, D., PELEKASIS, N.A. & TSAMOPOULOS, J. 2004 Spherical capsules in three-dimensional unbounded Stokes flows: effect of the membrane constitutive law and onset of buckling. *J. Fluid Mech.* **516**, 303–334.

LEES, A.W. & EDWARDS, S.F. 1972 The computer study of transport processes under extreme conditions. *J. Phys. C: Solid State Phys.* **5** (15), 1921.

LÓPEZ, H.M., GACHELIN, J., DOUARCHE, C., AURADOU, H. & CLÉMENT, E. 2015 Turning bacteria suspensions into superfluids. *Phys. Rev. Lett.* **115**, 028301.

MARCHETTI, M.C., JOANNY, J.F., RAMASWAMY, S., LIVERPOOL, T.B., PROST, J., RAO, M. & SIMHA, R.A. 2013 Hydrodynamics of soft active matter. *Rev. Mod. Phys.* **85**, 1143–1189.

MARTINEZ, V.A. *et al.*et al. 2020 A combined rheometry and imaging study of viscosity reduction in bacterial suspensions. *Proc. Natl Acad. Sci. USA* **117** (5), 2326–2331.

MATSUI, H., OMORI, T. & ISHIKAWA, T. 2020*a* Hydrodynamic interaction of two deformable torque swimmers. *J. Fluid Mech.* **894**, A9.

MATSUI, H., OMORI, T. & ISHIKAWA, T. 2020*b* Rheology of a dilute suspension of deformable microswimmers. *Phys. Fluids* **32** (7), 071902.

MATSUNAGA, D., IMAI, Y., YAMAGUCHI, T. & ISHIKAWA, T. 2016 Rheology of a dense suspension of spherical capsules under simple shear flow. *J. Fluid Mech.* **786**, 110–127.

MENZEL, A.M. & OHTA, T. 2012 Soft deformable self-propelled particles. *EPL (Europhys. Lett.)* **99** (5), 58001.

NESS, C., SETO, R. & MARI, R. 2022 The physics of dense suspensions. *Annu. Rev. Condens. Matt. Phys.* **13**, 97–117.

OMORI, T., IMAI, Y., YAMAGUCHI, T. & ISHIKAWA, T. 2012 Reorientation of a nonspherical capsule in creeping shear flow. *Phys. Rev. Lett.* **108**, 138102.

OMORI, T., ISHIKAWA, T., IMAI, Y. & YAMAGUCHI, T. 2013 Shear-induced diffusion of red blood cells in a semi-dilute suspension. *J. Fluid Mech.* **724**, 154–174.

PAGONABARRAGA, I. & LLOPIS, I. 2013 The structure and rheology of sheared model swimmer suspensions. *Soft Matt.* **9**, 7174–7184.

POZRIKIDIS, C. 1992 *Boundary Integral and Singularity Methods for Linearized Viscous Flow*. Cambridge University Press.

POZRIKIDIS, C. 2010 *Computational Hydrodynamics of Capsules and Biological Cells*, chap. 2, pp. 35–70. CRC Press.

RAFAÏ, S., JIBUTI, L. & PEYLA, P. 2010 Effective viscosity of microswimmer suspensions. *Phys. Rev. Lett.* **104**, 098102.

RUSSEL, W.B. 1980 Review of the role of colloidal forces in the rheology of suspensions. *J. Rheol.* **24** (3), 287–317.

SAINTILLAN, D. 2010 The dilute rheology of swimming suspensions: a simple kinetic model. *Expl Mech.* **50**, 1275–1281.

SAINTILLAN, D. 2018 Rheology of active fluids. *Annu. Rev. Fluid Mech.* **50**, 563–592.

SIEROU, A. & BRADY, J.F. 2002 Rheology and microstructure in concentrated noncolloidal suspensions. *J. Rheol.* **46** (5), 1031–1056.

SKALAK, R., TOZEREN, A., ZARADA, R.P. & CHIEN, S. 1973 Strain energy function of red blood cell membranes. *Biophys. J.* **13** (3), 245–264.

WALTER, J., SALSAC, A.V., BARTHES-BIESEL, D. & TALLEC, P.L. 2010 Coupling of finite element and boundary integral methods for a capsule in a Stokes flow. *Intl J. Numer. Meth. Engng* **83** (7), 829–850.

ZHANG, X. & GRAHAM, M.D. 2020 Multiplicity of stable orbits for deformable prolate capsules in shear flow. *Phys. Rev. Fluids* **5**, 023603.

https://doi.org/10.1017/jfm.2026.11965 Published online by Cambridge University Press